

<https://doi.org/10.1038/s41612-025-00912-5>

Reversed link between central pacific ENSO and Greenland–Barents sea ice

Yuxin Xie¹, Anmin Duan¹✉, Chao Zhang^{1,2}✉, Chuangzhi He¹, Qi Mao¹ & Bingxian Liu¹

Winter Arctic sea ice is a crucial climate indicator, declining at an accelerated rate compared to the past and playing a significant role in Arctic amplification over recent decades. The sea-ice concentration (SIC) in the Greenland–Barents Sea (GBS) shows considerable interannual variability, yet the link between this variability and the El Niño–Southern Oscillation (ENSO) remains uncertain. Here, we identify a reversed relationship between the autumn Central Pacific (CP)-type ENSO and the winter GBS SIC around the mid-1980s. Observational and model experiments demonstrate that, before the mid-1980s, CP ENSO triggered a double wave pattern propagating toward the Arctic, generating a positive geopotential height anomaly in the Arctic. Such an anomaly, along with a northerly anomaly, favored cold-air advection and intrusion into the GBS, resulting in an increased SIC. After the mid-1980s, however, CP ENSO only induced a single wave train towards the Arctic, favoring a positive geopotential height anomaly over Iceland. As a result, the southerly anomaly transported abundant moisture into the GBS and consequently reduced the SIC. The variation in wave patterns can largely be attributed to the sea surface temperature anomaly in the tropical Atlantic induced by CP ENSO. Our findings highlight the unstable connection between tropical and polar regions, which provides a basis for better understanding the mechanisms of Arctic sea-ice changes.

Arctic sea ice serves as a crucial indicator of global climate variability, being closely tied to various aspects of the Northern Hemisphere's climate^{1–5}. In recent decades, the Arctic sea ice has experienced a rapid decline^{6–8}, along with significant interannual variability^{9,10}. These changes stem from both dynamic processes, such as sea-ice drift and deformation, as well as thermodynamic processes, including sea-ice freezing and melting^{2,11–15}.

Ocean–atmosphere processes modulate the Arctic sea ice variability to a considerable degree^{2,14,16–18}. For instance, the El Niño–Southern Oscillation (ENSO) influences Arctic sea ice by causing tropical sea surface temperature (SST) anomalies that change the atmospheric circulation^{14,19}. The North Atlantic Oscillation, Ural Blocking, and snow cover on the Tibetan Plateau also drive changes in Arctic sea ice through thermal and dynamic mechanisms^{2,16}.

In the tropics, a shift in ENSO from the eastern Pacific (EP) to central Pacific (CP) type in recent decades (marked by a westward shift in the SST anomaly center and a shorter duration of SST anomalies)^{20–24} has led to changes in its teleconnection with the Arctic^{19,25}, and CP ENSO plays a more prominent role in Arctic warming^{19,25,26} and sea-ice changes¹⁹ compared with EP ENSO. However, the stability of the CP ENSO–Arctic sea ice relationship remains poorly understood. As such, this study aims to address this issue by

elucidating the association between the two and the atmospheric processes that affect the stability of this association. Specifically, our study focuses on the winter (December–January–February, DJF) Arctic sea ice, regarded as a driver of Arctic amplification^{27,28}, whose loss is occurring more rapidly than in the past²⁹. Moreover, ENSO typically develops and peaks in autumn and winter^{30,31}, and a recent study indicates a potential connection between ENSO and the interannual variability of winter Arctic sea ice¹⁴. We selected the Greenland–Barents Sea (GBS) as our study area because of its high winter sea-ice concentration (SIC)³² and strong interannual variability^{8,33}, and because the sea ice in this region has been shown to be associated with ENSO^{14,34}. We identified a nonsignificant correlation between GBS SIC and CP ENSO over a long period. However, their relationship is unstable and shows opposite results in different periods. This study highlights the fluctuating relationship between CP ENSO and GBS SIC, while also uncovering the potential underlying physical mechanisms.

Results

Reversal in the relationship between GBS SIC and CP ENSO

During 1950 to 2022, the winter SIC over the GBS (65°–85°N, 40°W–60°E) exhibits high values and strong interannual variability (Supplementary

¹Center for Marine Meteorology and Climate change, State Key Laboratory of Marine Environmental Science, College of Ocean and Earth Sciences, Xiamen University, Xiamen, China. ²Marine Biogeochemistry Division, GEOMAR Helmholtz Centre for Ocean Research Kiel, Kiel, Germany.

✉ e-mail: amduan@xmu.edu.cn; chaozhang@xmu.edu.cn

Fig. 1a and 1b), consistent with previous findings^{8,33}. To capture its spatial pattern, we computed the leading empirical orthogonal function mode (EOF1) of the winter SIC anomalies over the GBS (Supplementary Fig. 2a) and the corresponding principal component (PC1, Supplementary Fig. 2b). The spatial distribution reveals a high winter SIC anomaly over the GBS, along with strong interannual variability that fluctuates over time. However, this SIC variation shows a weak long-term correlation with the different types of ENSO during winter (Supplementary Fig. 4a).

As previous research has indicated, an unstable relationship between ENSO and the Arctic climate has occurred²⁵. In this study, a sliding correlation analysis with a 21-year window was used to examine the relationship between the GBS SIC PC1 and different ENSO indices during winter (Supplementary Fig. 3). The reversed correlation around the mid-1980s provides an explanation for the low SIC–ENSO correlation in the long term (Supplementary Fig. 4e) because of the offsetting from the opposite signs. We selected the NiñoCP index for this study because its correlation with GBS SIC is more significant than that of other indices (Supplementary Fig. 3). Notably, Niño 1 + 2, Niño 3, and Niño EP are positive and statistically significant more recently. Additionally, all the indices exhibit a positive–negative–positive decadal correlation signature. These issues remain to be further explored in future studies.

To further examine their relationship during the developing period of ENSO, we performed a lagged 21-year sliding correlation between the GBS SIC PC1 in winter and the NiñoCP index from autumn (September–October–November, SON) to winter. Our analysis highlighted that their significant correlation dates back to the preceding autumn (Fig. 1a). Moreover, the results are not sensitive to the length of the sliding window. Therefore, we selected the autumn NiñoCP index for subsequent analysis.

Based on the maximum-value points (1974 and 1996) from the sliding correlation coefficients, we divided the study period into two distinct intervals: 1964–1984 (P1, $R = 0.43$, $p < 0.05$) and 1986–2006 (P2, $R = -0.49$, $p < 0.05$). To confirm their inverse relationship, we calculated the spatial distribution of the NiñoCP-associated winter GBS SIC anomalies. In association with the positive phase of CP ENSO, significant positive and negative SIC anomalies can be observed over the GBS in P1 and P2, respectively (Fig. 1b, c), validating their reversed relationship between the two periods.

Differences in atmosphere–ocean interactions around the mid-1980s

The SST anomaly patterns associated with CP ENSO in P1 and P2 are depicted in Fig. 2a, b, respectively. Significant warm SST anomalies can be observed in the tropical North Atlantic in P1, whereas there are almost no SST anomaly signals in P2. The weakening impacts of ENSO on the tropical Atlantic SST were largely due to the reduced wind–evaporation–SST feedback caused by the westward shift of ENSO teleconnections after the mid-

1980s³⁵. Therefore, the varying SST forcings in the tropical North Atlantic suggest changes in atmospheric responses. As expected, during P1, significant convergent (Fig. 2i) and upward motion (Fig. 2e) anomalies associated with CP ENSO can be observed in the subtropical North Atlantic, resulting in localized increased precipitation anomalies (Fig. 2g). In contrast, during P2, the atmospheric responses in the subtropical North Atlantic are much weaker because of the reduced SST forcing (Fig. 2b, d, f, h, j).

Robust Rossby wave sources can be observed in the subtropical northeastern Pacific for both periods. Notably, during P1, the upper-level divergent wind (Fig. 2c) and positive precipitation (Fig. 2g) anomalies support the perturbation anomalies in the upper troposphere³⁶, which is crucial in the formation of Rossby wave sources in the subtropical North Atlantic (Fig. 2i). In contrast, during P2, weak Rossby wave source anomalies are due to the much weaker upper-level divergent wind (Fig. 2d) and precipitation (Fig. 2h) anomalies (Fig. 2j). These results indicate two Rossby wave source centers swept across the subtropical Pacific and Atlantic in P1, whereas only one center existed over the tropical Pacific in P2.

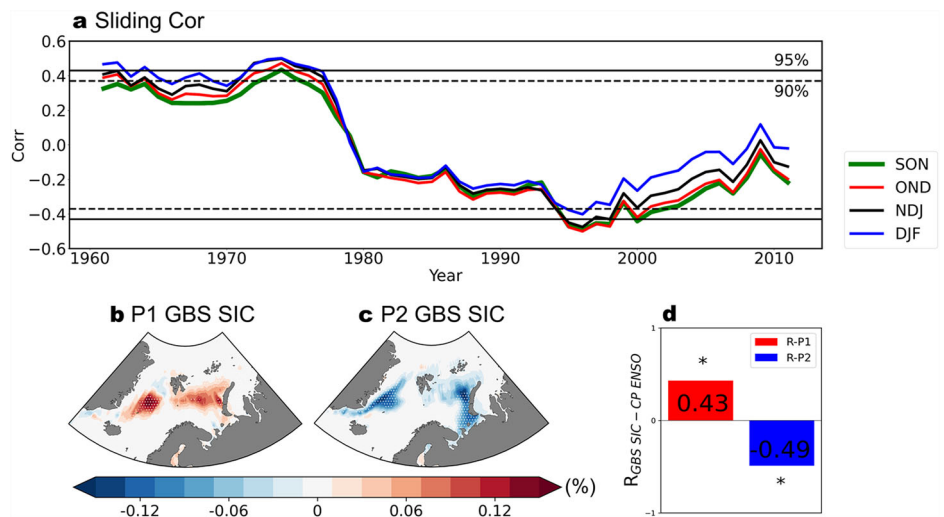
Different SST forcings induce various atmospheric teleconnections^{19,20,25,26}. To further understand these different responses, we calculated the height and wave activity flux (WAF) anomalies using both observations and model experiments (Fig. 3). Two control experiments and two corresponding sensitivity experiments were conducted using the Community Atmosphere Model, version 6.0 (CAM6; see Methods for details). In this study, the CAM6 responses were calculated as the differences between the sensitivity and control experiments. During P1, both observations and model experiments show that significant negative geopotential height anomalies dominate in the subtropical Pacific and Atlantic Ocean (Fig. 3), which is consistent with the SST forcing there (Fig. 2a, b), due to the tropical Gill response³⁷. The WAFs propagate from these two oceans towards the Arctic (Fig. 3a, c), indicating two pathways of the atmospheric wave train resulting from the double Rossby wave sources.

In comparison, during P2, significant negative geopotential height anomalies prevail over the subtropical Pacific (Fig. 3b, d), which aligns with the single SST forcing there (Fig. 2b). The corresponding wave flux travels from the North Pacific, across North America, and extends to the North Atlantic, indicating an atmospheric waviness due to the single Rossby wave source (Fig. 2j). Notably, in the atmospheric wave trains, clear geopotential height anomalies appear over northern Canada and Greenland in P1, while positive anomalies prevail across Iceland in P2. These different locations of geopotential height anomalies indicate distinct influences on the GBS climate anomalies.

Physical processes of ENSO's impact on the Arctic SIC

The above analysis implies that positive geopotential height anomalies in the Arctic associated with CP ENSO (i.e., anticyclonic anomalies, Supplementary

Fig. 1 | Shift in the relationship between GBS SIC and CP ENSO. **a** The 21-year sliding correlation between different Niño indices and the PC1 of GBS SIC. The green, red, purple, and blue lines represent the SON (September to November), OND (October to December), NDJ (November to January), and DJF (December to February) sliding correlation coefficients, respectively. The black solid (dashed) line represents the 95% (90%) confidence level. DJF GBS SIC (%) anomalies regressed onto the SON NiñoCP index during **(b)** 1964–1984 (P1) and **(c)** 1986–2006 (P2). **d** Correlation coefficients between CP ENSO and GBS SIC in P1 and P2. The dotted regions and asterisks indicate statistical significance at the 95% confidence level based on a two-tailed Student's *t*-test.



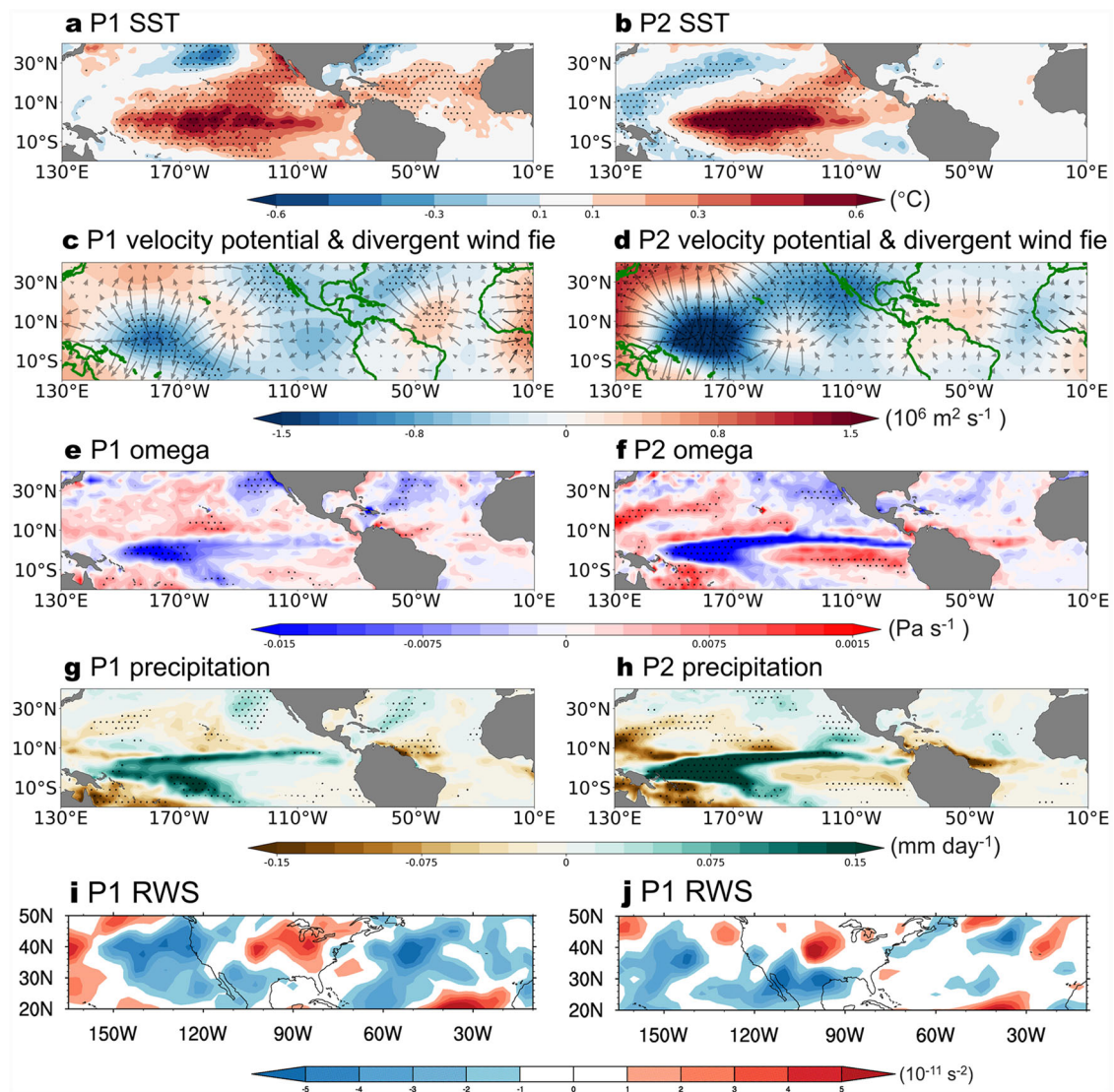


Fig. 2 | Differences in the air-sea interactions associated with CP ENSO. DJF (a, b) SST (color shading, $^{\circ}\text{C}$), (c, d) 200 hPa velocity potential (color shading, $10^6 \text{ m}^2 \text{ s}^{-1}$) and divergent wind (vectors, m s^{-1}), (e, f) 850 hPa vertical velocity (color shading, mm s^{-1}), (g, h) 850 hPa precipitation (color shading, mm d^{-1}), (i, j) 200 hPa Rossby wave source (RWS, color shading, 10^{-11} s^{-2}) anomalies regressed onto the SON NiñoCP index during (a, e, g, i) 1964–1984 (P1) and (b, f, h, j) 1986–2006 (P2). The dotted regions indicate statistical significance at the 95% confidence level based on a two-tailed Student's *t*-test.

Fig. 3 | Observational and modeled responses of geopotential height and WAF anomalies to different SST forcings. DJF 200 hPa geopotential height (color shading, gpm) and WAF (streamlines) regressed onto the SON NiñoCP index during (a) in 1964–1984 (P1) and (b) in 1986–2006 (P2). c, d As in (a, b) but for the CAM6 model experiments. The dotted regions indicate statistical significance at the 95% confidence level based on a two-tailed Student's *t*-test.

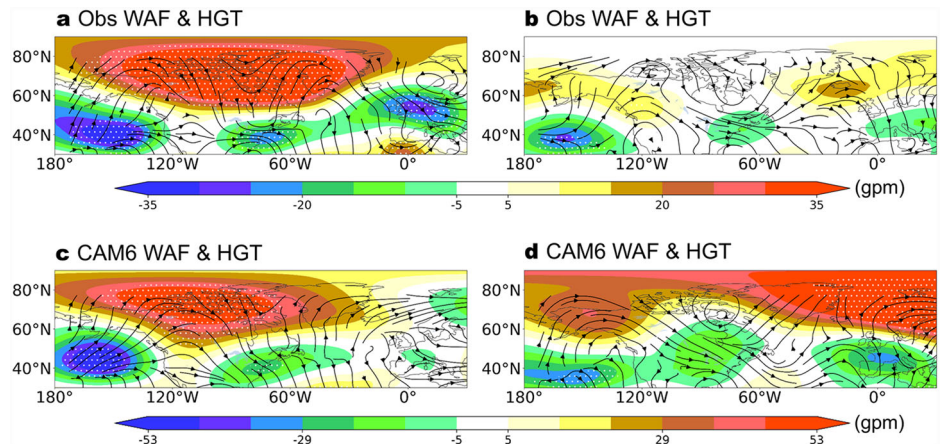


Fig. 4 | Different GBS thermal processes associated with changes in CP ENSO. DJF (a–d) 925 hPa water vapor flux (vectors, $\text{kg m}^{-1} \text{s}^{-1}$) and specific humidity (color shading, g kg^{-1}) and (e–h) SAT (K) regressed onto the SON NiñoCP index during (a, e) 1964–1984 (P1) and (b, f) 1986–2006 (P2). c, d, g, h As in (a, b, e, f) but for the CAM6 model experiments. The dotted regions indicate statistical significance at the 95% confidence level based on a two-tailed Student's *t*-test.

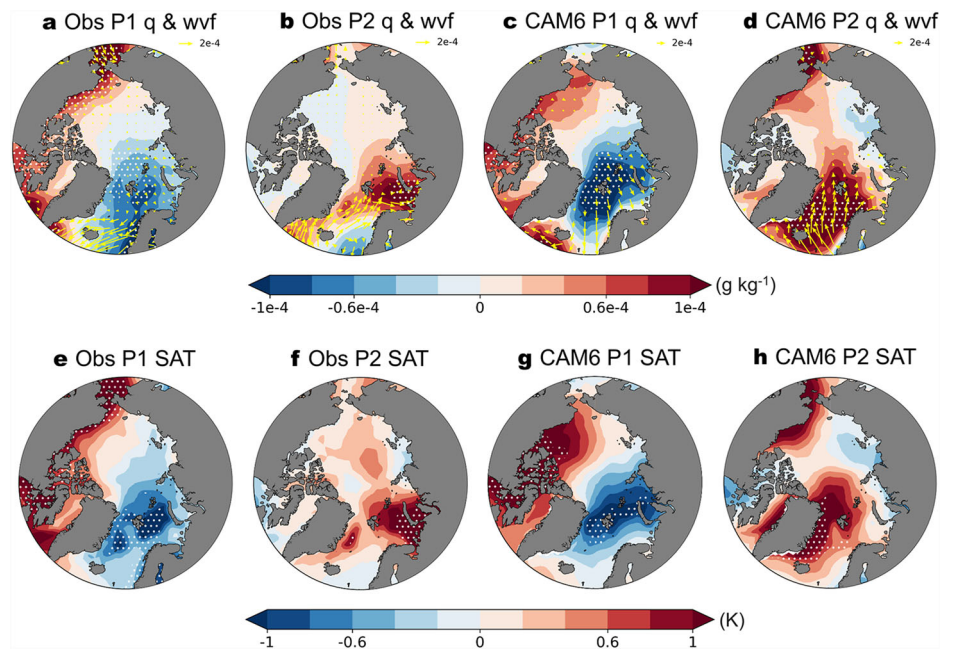


Fig. 5 | Changes in the mechanisms of impact of CP ENSO on GBS SIC. In 1964–1984 (P1), SST anomalies in the tropical Pacific and Atlantic stimulated two Rossby wave trains, leading to positive geopotential height anomalies over northern Canada and Greenland. This resulted in dry, cold Arctic air invading the GBS, causing sea-ice growth. In 1986–2006 (P2), SST anomalies in the tropical Pacific generated one Rossby wave train, leading to positive geopotential height anomalies over Iceland. This brought warm, humid air from the North Atlantic into the GBS, resulting in a reduction of sea ice.

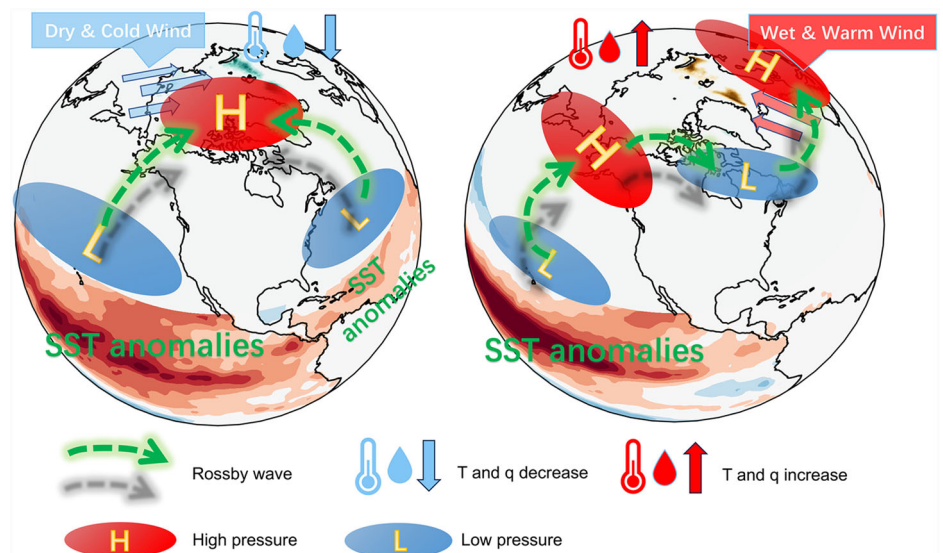


Fig. 5) are the key system impacting the GBS climate anomalies. Observations and model experiments suggest that, during P1, on the eastern flank of the anticyclone, the northerly anomalies transported Arctic cold air towards the GBS (Supplementary Fig. 6a) and inhibited moisture intrusion into the GBS (Fig. 4a, c), resulting in SIC growth (Fig. 1b) by cooling the surface air temperature (SAT; Fig. 4e, g). ENSO tends to yield a positive mid-tropospheric height relationship and southerly winds over the GBS during P2. This center of action is located over the high-latitude North Atlantic, is downstream of the P1 high pressure center, and is of weaker magnitude (and not significant) compared with the pattern observed during P1. On the western flank of the anticyclone, southerly anomalies favored warm advection (Supplementary Fig. 6b) and water vapor transport from the North Atlantic to the GBS (Fig. 4b, d), which promoted SIC melting (Fig. 1c) by warming the SAT (Fig. 4f, h).

Regarding the dynamic process of sea ice (Supplementary Fig. 7), in P1, ENSO-related sea-ice drifts equatorward, facilitating the transport of highly concentrated sea ice from the center of the Arctic to the GBS, resulting in sea-ice accumulation (Supplementary Fig. 7a). On the contrary, in P2, the

ENSO-related sea-ice motion shows that part of the sea ice moves away from the GBS towards the North Atlantic, leading to a decrease in SIC (Supplementary Fig. 7b). The above results suggest that CP ENSO can affect GBS SIC anomalies through both thermal and dynamic processes.

Summary and discussion

This study reveals an unstable link between CP ENSO and GBS SIC around the mid-1980s. The process by which CP ENSO influences GBS SIC is demonstrated using observations and model experiments. Our findings indicate that the tropical Atlantic SST response to CP ENSO is a key factor in the reversal of the CP ENSO–GBS SIC connection.

The pathways of CP ENSO's influence on the GBS SIC are illustrated in Fig. 5. In P1, the SST anomalies in the Pacific and Atlantic Ocean stimulated a double Rossby wave pattern propagating toward the Arctic, ultimately causing increased GBS SIC due to the intrusion of dry and cold air from the center of the Arctic. In P2, because of the weak SST anomaly in the Atlantic Ocean, only one Rossby wave source was stimulated, which then propagated toward the

GBS. Ultimately the intrusion of warm and humid air from the North Atlantic led to decreased GBS SIC. Additionally, the Arctic winter warm bias caused by CAM6's overestimation of the cloud fraction and the amount of cloud liquid water, along with its underestimation of autumn snow cover, may impact the atmospheric circulation and potentially explain the stronger positive geopotential height anomaly in P2 compared to observations^{38,39}.

In this study, we focused on the relationship between CP ENSO and GBS SIC from an atmospheric perspective. However, oceanic processes significantly influence sea ice as well^{40,41}. Over longer time scales, understanding the connection between ENSO-related oceanic processes and Arctic sea ice is of great research significance¹⁴. This question remains unexplored and requires further research.

Methods

Data

The study period spans 1950–2022. The monthly SST and SIC data on 1° grids are from the Hadley Center Sea Ice and Sea Surface Temperature dataset (HadISST). In addition, data with an interpolated horizontal resolution of $1^\circ \times 1^\circ$ from the National Snow and Ice Data Center (NSIDC) are used to verify the reliability of the SIC data. The monthly data (including winds, geopotential height, specific humidity, SAT, precipitation, and vertical motion), with an interpolated horizontal resolution of $2.5^\circ \times 2.5^\circ$, were downloaded from the fifth major global reanalysis produced by ECMWF (ERA5).

The monthly sea-ice motion data were sourced from the ECMWF's Ocean ReAnalysis System 5 (ORS5), spanning from 1958 to 2022 with a spatial resolution of $1^\circ \times 1^\circ$. The Niño indices used in this study are from the National Oceanic and Atmospheric Administration (NOAA).

In order to avoid the possible statistical influence of a climate trend^{42–44} or decadal variability^{35,45}, the datasets used in this paper were all detrended.

EOF analysis

An EOF analysis of the linearly detrended DJF GBS SIC anomalies during 1950–2022 was performed to extract the EOF1 mode of the interannual GBS SIC anomaly by computing the eigenvectors of a spatially weighted anomaly covariance matrix. The corresponding PC1 time series represents the interannual variability of GBS SIC. The EOF1 pattern and PC1 of sea-ice data from NSIDC and HadISST show a high correlation, which indicates that the results in this study are reliable.

Definitions of CP ENSO and EP Niño indices

The NiñoEP and CP indices are defined as in Ren et al.³⁶:

$$\begin{cases} N_{CT} = N_3 - \alpha N_4 \\ N_{WP} = N_4 - \alpha N_3, \end{cases} \quad \alpha = \begin{cases} 2/5, & N_3 N_4 > 0 \\ 0, & \text{otherwise} \end{cases}, \quad (1)$$

where N_3 and N_4 represent the Niño3 and Niño4 indices, respectively.

RWS

The RWS⁴⁶ was calculated to diagnose the generation of Rossby wave trains:

$$S = -\nabla_H \cdot [\mathbf{u}'_x(f + \bar{\zeta})] - \nabla_H \cdot [\bar{\mathbf{u}}_x \zeta'], \quad (2)$$

where $\mathbf{u}_x = (\mathbf{u}_x, \mathbf{v}_x)$, in which \mathbf{u}_x and \mathbf{v}_x represent the longitudinal and latitudinal components of the divergent wind, respectively; and ∇_H , $\bar{\zeta}$ and $f + \bar{\zeta}$ denote the horizontal gradient, relative vorticity, and absolute vorticity, respectively.

WAF

The WAF is used to describe the propagation of atmospheric wave trains⁴⁷ and is expressed in pressure coordinates as follows:

$$W = \frac{1}{2|\mathbf{U}|} \left(\frac{U(\varphi_x'^2 - \varphi'_x \varphi_{xx}') + V(\varphi'_x \varphi_y' - \varphi'_x \varphi_{xy}')}{U(\varphi'_x \varphi_y' - \varphi'_x \varphi_{xy}') + V(\varphi_y'^2 - \varphi'_y \varphi_{yy}')} \right), \quad (3)$$

where $\mathbf{u} = (U, V)$ represents the latitudinal and longitudinal components of geostrophic wind; φ denotes the three-dimensional stream function; and the prime symbol and subscripts indicate deviations from the time and partial derivatives, respectively.

Statistical significance test

In this study, we employed Student's *t*-test to assess the statistical significance of the anomalous fields and correlation coefficients.

CAM6 experiments

CAM6, which is the atmospheric component of the Community Earth System Model, version 2.1.3 (CESM2.1.3), was employed to verify the teleconnection link and causal relationship between CP ENSO and the GBS regional climate in the two phases. The configuration “f09_f09_mg17”, which has a horizontal resolution of $0.9^\circ \times 1.25^\circ$ and 32 hybrid vertical layers, and the component “F2000_climo”, were selected in this study. The control experiments were forced with the monthly SST climatology by averaging the HadISST data over the periods 1964–1984 and 1986–2006. The model was integrated for 30 years, and the first 5 years were discarded. In the sensitivity experiments, we incorporated the anomalous SST from P1 and P2 (as shown in Fig. 2a, b, without amplitude scaling) into the climatological SST for the SONDJF period for each of the 25 cases. We then ran the model for six consecutive months (SONDJF) and selected the last three months (DJF) for analysis.

Code availability

Codes used in this study are available from the corresponding author on reasonable request.

Received: 7 October 2024; Accepted: 9 January 2025;

Published online: 21 January 2025

References

- Intergovernmental Panel on Climate, C. *Climate Change 2022 – Impacts, Adaptation and Vulnerability*. (2023).
- Zhang, C., Duan, A., Jia, X., Wang, Z. & Pan, Z. A dynamic link between spring Arctic sea ice and the Tibetan Plateau snow increment indicator. *npj Clim. Atmos. Sci.* **6**, 191 (2023).
- Wu, B., Su, J. & Zhang, R. Effects of autumn–winter Arctic sea ice on winter Siberian High. *Chin. Sci. Bull.* **56**, 3220–3228 (2011).
- Chen, S., Wu, R. & Chen, W. Enhanced impact of Arctic sea ice change during boreal autumn on the following spring Arctic oscillation since the mid-1990s. *Clim. Dyn.* **53**, 5607–5621 (2019).
- Wu, Z., Li, X., Li, Y. & Li, Y. Potential influence of Arctic sea ice to the interannual variations of East Asian spring precipitation. *J. Clim.* **29**, 2797–2813 (2016).
- Stroeve, J. C. et al. Trends in Arctic sea ice extent from CMIP5, CMIP3 and observations. *Geophys. Res. Lett.* **39**, 16 (2012).
- Serreze, M. C. & Stroeve, J. Arctic sea ice trends, variability and implications for seasonal ice forecasting. *Philos. Trans. R. Soc. A: Math., Phys. Eng. Sci.* **373**, 20140159 (2015).
- Cavalieri, D. J. & Parkinson, C. L. Arctic sea ice variability and trends, 1979–2010. *Cryosphere* **6**, 881–889 (2012).
- Laxon, S., Peacock, N. & Smith, D. High interannual variability of sea ice thickness in the Arctic region. *Nature* **425**, 947–950 (2003).
- Hao, G., Su, J., Vihma, T. & Huang, F. Trends, abrupt shifts and interannual variability of the Arctic wintertime seasonal sea ice from 1979 to 2019. *Ann. Glaciol.* **61**, 441–453 (2020).
- Jenkins, M. & Dai, A. The impact of Sea-Ice loss on Arctic climate feedbacks and their role for Arctic Amplification. *Geophys. Res. Lett.* **48**, e2021GL094599 (2021).
- Pithan, F. & Mauritsen, T. Arctic amplification dominated by temperature feedbacks in contemporary climate models. *Nat. Geosci.* **7**, 181–184 (2014).

13. Zhang, P. et al. More frequent atmospheric rivers slow the seasonal recovery of Arctic sea ice. *Nat. Clim. Change* **13**, 266–273 (2023).
14. Luo, B. et al. Origins of Barents-Kara sea-ice interannual variability modulated by the Atlantic pathway of El Niño–Southern Oscillation. *Nat. Commun.* **14**, 585 (2023).
15. Olonscheck, D., Mauritsen, T. & Notz, D. Arctic sea-ice variability is primarily driven by atmospheric temperature fluctuations. *Nat. Geosci.* **12**, 430–434 (2019).
16. Luo, B., Luo, D., Wu, L., Zhong, L. & Simmonds, I. Atmospheric circulation patterns which promote winter Arctic sea ice decline. *Environ. Res. Lett.* **12**, 054017 (2017).
17. Sumata, H., de Steur, L., Divine, D. V., Granskog, M. A. & Gerland, S. Regime shift in Arctic Ocean sea ice thickness. *Nature* **615**, 443–449 (2023).
18. Zhang, J. et al. Responses of Arctic sea ice to stratospheric ozone depletion. *Sci. Bull.* **67**, 1182–1190 (2022).
19. Hu, C. et al. Shifting El Niño inhibits summer Arctic warming and Arctic sea-ice melting over the Canada Basin. *Nat. Commun.* **7**, 11721 (2016).
20. Kug, J.-S., Jin, F.-F. & An, S.-I. Two types of El Niño events: cold tongue El Niño and warm pool El Niño. *J. Clim.* **22**, 1499–1515 (2009).
21. Ashok, K., Behera, S. K., Rao, S. A., Weng, H. & Yamagata, T. El Niño Modoki and its possible teleconnection. *J. Geophys. Res.: Oceans* **112**, C11 (2007).
22. Larkin, N. K. & Harrison, D. On the definition of El Niño and associated seasonal average US weather anomalies. *Geophys. Res. Lett.* **32**, 13 (2005).
23. Wang, C. & Weisberg, R. H. The 1997–98 El Niño evolution relative to previous El Niño events. *J. Clim.* **13**, 488–501 (2000).
24. Yu, J. Y. & Kao, H. Y. Decadal changes of ENSO persistence barrier in SST and ocean heat content indices: 1958–2001. *J. Geophys. Res. Atmos.* **112**, D13 (2007).
25. Wang, C., Ren, B., Yang, C., Zheng, J. & Jiang, L. Change of the CP ENSO's role in the occurrence frequency of Arctic daily warming events triggered by Atlantic storms. *npj Clim. Atmos. Sci.* **6**, 83 (2023).
26. Li, Z. et al. Different effects of two ENSO types on Arctic surface temperature in boreal winter. *J. Clim.* **32**, 4943–4961 (2019).
27. Screen, J. A. & Simmonds, I. The central role of diminishing sea ice in recent Arctic temperature amplification. *Nature* **464**, 1334–1337 (2010).
28. Dai, A., Luo, D., Song, M. & Liu, J. Arctic amplification is caused by sea-ice loss under increasing CO₂. *Nat. Commun.* **10**, 121 (2019).
29. Stroeve, J. & Notz, D. Changing state of Arctic sea ice across all seasons. *Environ. Res. Lett.* **13**, 103001 (2018).
30. Rasmusson, E. M. & Carpenter, T. H. Variations in tropical sea surface temperature and surface wind fields associated with the Southern Oscillation/El Niño. *Monthly Weather Rev.* **110**, 354–384 (1982).
31. Larkin, N. K. & Harrison, D. ENSO warm (El Niño) and cold (La Niña) event life cycles: Ocean surface anomaly patterns, their symmetries, asymmetries, and implications. *J. Clim.* **15**, 1118–1140 (2002).
32. Overland, J. E. & Wang, M. Future regional Arctic sea ice declines. *Geophys. Res. Lett.* **34**, 17 (2007).
33. Germe, A., Houssais, M. N., Herbaut, C. & Cassou, C. Greenland Sea sea ice variability over 1979–2007 and its link to the surface atmosphere. *J. Geophys. Res. Oceans* **116**, C10 (2011).
34. Chen, S., Wu, R., Chen, W. & Yu, B. Influence of winter Arctic sea ice concentration change on the El Niño–Southern Oscillation in the following winter. *Clim. Dyn.* **54**, 741–757 (2020).
35. Elsner, J. B., Bossak, B. H. & Niu, X. F. Secular changes to the ENSO–US hurricane relationship. *Geophys. Res. Lett.* **28**, 4123–4126 (2001).
36. Ren, H. L. & Jin, F. F. Niño indices for two types of ENSO. *Geophys. Res. Lett.* **38**, 4 (2011).
37. Gill, A. E. Some simple solutions for heat-induced tropical circulation. *Q. J. R. Meteorol. Soc.* **106**, 447–462 (1980).
38. Webster, M., DuVivier, A., Holland, M. & Bailey, D. Snow on Arctic sea ice in a warming climate as simulated in CESM. *J. Geophys. Res.: Oceans* **126**, e2020JC016308 (2021).
39. Baek, E.-H. et al. Characteristics of high-latitude climate and cloud simulation in Community Atmospheric Model Version 6 (CAM6). *Atmosphere* **13**, 936 (2022).
40. Polyakov, I. V. et al. Fluctuating Atlantic inflows modulate Arctic atlantification. *Science* **381**, 972–979 (2023).
41. Årthun, M., Eldevik, T., Smedsrud, L., Skagseth, Ø. & Ingvaldsen, R. Quantifying the influence of Atlantic heat on Barents Sea ice variability and retreat. *J. Clim.* **25**, 4736–4743 (2012).
42. Emanuel, K. Increasing destructiveness of tropical cyclones over the past 30 years. *Nature* **436**, 686–688 (2005).
43. Webster, P. J., Holland, G. J., Curry, J. A. & Chang, H.-R. Changes in tropical cyclone number, duration, and intensity in a warming environment. *Science* **309**, 1844–1846 (2005).
44. Holland, G. J. & Webster, P. J. Heightened tropical cyclone activity in the North Atlantic: Natural variability or climate trend? *Philos. Trans. R. Soc. A: Math., Phys. Eng. Sci.* **365**, 2695–2716 (2007).
45. Goldenberg, S. B., Landsea, C. W., Mestas-Núñez, A. M. & Gray, W. M. The recent increase in Atlantic hurricane activity: Causes and implications. *Science* **293**, 474–479 (2001).
46. Sardeshmukh, P. D. & Hoskins, B. J. The generation of global rotational flow by steady idealized tropical divergence. *J. Atmos. Sci.* **45**, 1228–1251 (1988).
47. Takaya, K. & Nakamura, H. A formulation of a phase-independent wave-activity flux for stationary and migratory quasigeostrophic eddies on a zonally varying basic flow. *J. Atmos. Sci.* **58**, 608–627 (2001).

Acknowledgements

We thank Dr Yuheng Tang, Zhulei Pan, Shutao Cao, Xianyi Yang, Guanqi Fu, Chunyan Xiao, Qi Mao for their technical supports and Dr Yuzhuo Peng for her helpful comments. This work was funded by the National Natural Science Foundation of China (42305016, 42030602) and the Fundamental Research Funds for the Central Universities (20720240006). Chao Zhang was supported by the Chinese Scholarship Council (File No. 202306310194) and the Outstanding Postdoctoral Scholarship, State Key Laboratory of Marine Environmental Science at Xiamen University.

Author contributions

C.Z. developed the concept and designed the study; Y.X. designed the CAM6 experiments and plotted the figures; C.Z., Y.X., and A.D. performed formal analyses; Y.X. and C.Z. drafted the initial manuscript; A.D. and C.Z. provided funding; A.D., C.Z., C.H., and B.L. provided comments and revised the manuscript.

Competing interests

The authors declare no competing interests.

Additional information

Supplementary information The online version contains supplementary material available at <https://doi.org/10.1038/s41612-025-00912-5>.

Correspondence and requests for materials should be addressed to Anmin Duan or Chao Zhang.

Reprints and permissions information is available at <http://www.nature.com/reprints>

Publisher's note Springer Nature remains neutral with regard to jurisdictional claims in published maps and institutional affiliations.

Open Access This article is licensed under a Creative Commons Attribution-NonCommercial-NoDerivatives 4.0 International License, which permits any non-commercial use, sharing, distribution and reproduction in any medium or format, as long as you give appropriate credit to the original author(s) and the source, provide a link to the Creative Commons licence, and indicate if you modified the licensed material. You do not have permission under this licence to share adapted material derived from this article or parts of it. The images or other third party material in this article are included in the article's Creative Commons licence, unless indicated otherwise in a credit line to the material. If material is not included in the article's Creative Commons licence and your intended use is not permitted by statutory regulation or exceeds the permitted use, you will need to obtain permission directly from the copyright holder. To view a copy of this licence, visit <http://creativecommons.org/licenses/by-nc-nd/4.0/>.

© The Author(s) 2025